The nanoindentation responses of nickel surfaces with different crystal orientations

S.-P. Ju [a] , C.-T. Wang [a] , C.-H. Chien [a] , J. C. Huang [b] & S.-R. Jian [c]

[a] Department of Mechanical and Electro-Mechanical Engineering , Center for Nanoscience and Nanotechnology, National Sun-Yat-Sen University , Kaohsiung, 804, Taiwan

[b] Institute of Materials Science and Engineering; Center for Nanoscience and Nanotechnology, National Sun-Yat-Sen University , Kaohsiung, 804, Taiwan

[c] Department of Electrophysics , National Chiao Tung University , Hsinchu, 300, Taiwan
Published online: 27 Jul 2010.

PLEASE SCROLL DOWN FOR ARTICLE

Taylor & Francis
Taylor & Francis Group

The nanoindentation responses of nickel surfaces with different crystal orientations

S.-P. JU†*, C.-T. WANG†, C.-H. CHIEN†, J. C. HUANG‡ and S.-R. JIAN¶

†Department of Mechanical and Electro-Mechanical Engineering, Center for Nanoscience and Nanotechnology, National Sun-Yat-Sen University, Kaohsiung 804, Taiwan
‡Institute of Materials Science and Engineering; Center for Nanoscience and Nanotechnology, National Sun-Yat-Sen University, Kaohsiung 804, Taiwan
¶Department of Electrophysics, National Chiao Tung University, Hsinchu 300, Taiwan

Molecular dynamics (MD) simulations are applied to elucidate the anisotropic characteristics in the material responses for crystallographic nickel substrates with (100), (110) and (111) surface orientations during nanoindentation, compensating for the experimental limitation of nanoindentation—particularly for pure nickel substrates of three crystallographic orientations. This study examines several factors under indentation: three-dimensional phases of plastic deformation which correspond to atomic stress distributions, pile-up patterns at maximum indentation depth, and extracted material properties at different crystallographic orientations. The present results reveal that the strain energy of the substrate exerted by the tip is stored by the formation of the homogeneous nucleation, and is dissipated by the dislocation sliding of the {111} plane. The steep variations of the indentation curve from the local peak to the local minimums are affected by the numbers of slip angle of {111} sliding plane. The pile-up patterns of the three nickel substrates prove that the crystalline nickel materials demonstrate the pile-up phenomenon from nanoindentation on the nano-scale. The three crystallographic nickel substrates exhibit differing amounts of pile-up dislocation spreading at different crystallographic orientations. Finally, the effects of surface orientation in material properties of FCC nickel material on the nano-scale are observable through the slip angle numbers of {111} sliding planes which influence hardness values, as well as the cohesive energy of different crystallographic surfaces that indicate Young's modulus.

Keywords: Molecular dynamics; Nanoindentation; Nickel; Orientation effect; Dislocation; Pile-up; Hardness; Elastic modulus

1. Introduction

Recently, considerable attention has been devoted to atomic-scale processes and the measurable techniques of materials. Specifically, the material properties of substrates of nano-scale thickness have received attention because of the specific characteristics of their mechanical and physical properties [1,2]. Nickel is one of the favoured materials for either reactively or catalytically forming a smooth electroless deposition of additional thin layers in order to provide enhanced magnetic read–write capability on magnetic memory disks [3,4]. In micro electro-mechanical system (MEMS) application, nickel has been found to have excellent mechanical and magnetic properties that can be exploited to realize movable structures [5–8]. At this small scale, the macro-scale deformation of the bulk material will be less significant than the influences of different local atomic arrangement or the surface orientation upon which a nano-scale deformation mechanism imposes an external force [9]. This study examines the relationships between material properties and deformation mechanisms of surfaces of different crystallographic orientations under nano-scale, because they can provide significant information for the manufacture and design of nano-components, one of nanotechnology's promising applications.

In general, mechanical properties such as the elastic modulus and hardness of the nano-thin film can be measured by nanoindentation techniques. In recent years, the measurement of the operation specimen by nanoindentation techniques was fallen below the level of 100 nm [10,11]. Accordingly, these techniques provide researchers an excellent opportunity to obtain the characteristics of the material properties of nano-thin films. However,

*Corresponding author. Email: jushin-pon@mail.nsysu.edu.tw

the experimental method of nanoindentation measurement on nano-thin films is not easy to accomplish, both because the experimental techniques are on the atomic-scale level, and because it is difficult to investigate the transient atomic information inside the specimen during the nanoindentation process. Therefore, theoretical methods can accompany experimental techniques to provide much useful information without the limitations of the experimental method. Though the theoretical method is useful for analysis of nanoindentation on the nano-scale, it must be passed through the numerical method in order to completely observe the variations in the process of nanoindentation. Correspondingly, molecular dynamics (MD) simulation, which is suitable for nanoindentation analysis under nano-scale, is a powerful numerical method to describe the detailed variations at the atomic-scale.

MD simulation studies were initiated in the late 1950s at the Lawrence Radiation Laboratory (LRL) by Alder and Wainwright [12–13] in the field of equilibrium and non-equilibrium statistical mechanics. The application of MD simulation to the cutting and indentation process was first introduced at Lawrence Livermore National Laboratory (LLNL) in the late 1980s and early 1990s [14,15]. Pioneering research in the field of MD simulations of indentation was conducted by Landman *et al.* [16–19] at the Georgia Institute of Technology, followed by Belak and his colleagues at the LLNL. Since then, MD simulation has been applied to a wide range of fields, including crystal growth, low-pressure diamond synthesis, laser interactions, nanometric cutting [20–26], indentation [27–31] and tribology [32–36]. Nowadays, MD methods using empirical interatomic potentials can be implemented in simulating large-scale systems of up to ten million atoms [37–38]. However, because of the limitation of the experimental indentation equipment, research is rarely published that focuses on the influence of different surface orientations on the mechanical properties of the indentation substrate during nanoindentation. Even for MD simulations, there are no complete and systematic discussions on this topic. In related studies, Mante *et al.* [39] performed an investigation of the elastic modulus and hardness of selected crystallographic planes of single crystal titanium using a mechanical properties microprobe (MPM). Gouldstone *et al.* [10] utilized nanoindentation experiments on thin film of polycrystalline aluminium of known texture and different thicknesses, and of single crystal aluminium of different crystallographic orientations. Wang *et al.* [40] presented a study about the dependence of nanoindentation pile-up patterns and of micro-textures on the crystallographic orientation using high purity copper single crystals. Komanduri *et al.* [36] utilized MD simulations of nanoindentation followed by nanoscratching conducted on single crystal aluminium (with the crystal set up in the (001) [100] orientation and with scratching performed in the [100] direction) at extremely fine scratch depths (from 0.8 nm to near zero) to investigate atomic-scale friction. Subsequently, Komanduri *et al.* [41] used MD

simulations to investigate the effect of crystallographic factors (crystal orientation and direction of scratching) in indentation and scratching conducted on single crystal aluminium at specific combinations of orientations {(111), (110), (001), ($\bar{1}$20)} and scratch directions $<$ [$\bar{1}$10], [$\bar{2}$11], [100], [210], [221] $>$. Kum [42] performed MD simulations to study anisotropic features in nano-mechanical properties at the surface of nickel single crystals as a function of indenter size and velocity for three crystallographic orientations: (100), (110) and (111).

For the previously mentioned research, although Komanduri [36,41] performed MD simulations of nanoindentation to study the influences of crystallographic factors on FCC metals in indentation and scratching, the only material used in the simulated models is single crystal aluminium. Moreover, the atomic phases depicting deformation in the simulated models are only presented in 2D morphologies, and neither the homogeneous nucleation nor the dislocation sliding of plastic deformation are clearly visible during indentation and scratching. In addition, although Kum [42] performed MD simulations to investigate the orientation effects of elastic–plastic deformation on (100), (110), and (111) crystallographic orientations of nickel substrates—which is similar to our current investigation—the main aim of Kum's research was to calculate the parameters of power law on the initial stage of the indentation curve in order to obtain the nano-mechanical properties of elastic deformation. The plastic deformation characteristics of dislocation and nucleation in the course of indentation were not presented in the study, and the influences of three crystallographic orientations on the mechanical properties of both the hardness and the elastic modulus were not discussed [42]. Therefore, the main purpose of this paper is to use MD simulations of nanoindentation to analyse the influences of both plastic deformation characteristics and of atomic stress variations on the material properties of different crystallographic nickel substrates during nanoindentation. The notable results of our research include the presentation of 3D atomic phases of plastic deformation induced by indentation corresponding to atomic stress distributions, diagrams of the pile-up patterns at the maximum indentation depth, and the extracted material properties from the indentation curves for (100), (110) and (111) crystallographic orientations of nickel substrates in the course of nanoindentation.

2. Simulation methodology

The simulated models consist of (100), (110) and (111) crystallographic orientation surfaces and three monocrystalline nickel substrates. The dimensional scales of the simulated models are approximately $125 \times 125 \times 155$ Å. The simulated functions consist of the rigidity, thermostat and Newtonian functions from the method utilized by Jeng

et al. [43]. The rigidity atoms at the fixed bottom layers of substrate are assumed to be unaffected by the tip during the indentation process. Therefore, they are fixed in their initial atomic positions so as to maintain the complete frame for the simulated model. Periodic boundary conditions are used in the transverse x and y directions, which represent the infinite boundary of the substrate. The sharp tip of the indenter has a conical shape with a diameter of 6 nm and height of 3 nm. To acquire the most efficient calculations, the tip atoms also are assumed to be the same as the rigidity atoms; however, the tip atoms' indentation velocity is given by the displacement-rate at each time step of the simulation for the force interaction between the tip and the substrates.

The motions of thermostat atoms are modified based on Nosé-Hoover thermostat [44], which sets up a heat bath that controls the temperature of Newtonian atoms to ensure the average temperature is at the desired value. The motions of all Newtonian atoms are determined by the interatomic forces derived by the interaction potential. The rigidity atoms of the nickel substrate are arranged as the fixed bottom layers, and the thermostat atoms are arranged on top of the fixed bottom layers. Meanwhile, the Newtonian atoms of the nickel substrate at the top region are bound by the thermostat atoms and are free to move by the influence of the tip atoms. The indenter tip is positioned on the top of the substrate surface at the centre, held at a constant distance from the substrate before the commencement of the indentation process. Because the three substrates are composed of more than 140,000 nickel atoms in each simulated model, we implement parallel computations by using the atom decomposition method [45]. The configurations of the simulated model are shown in figure 1.

In the present simulations, the interatomic force derived from the potential function is described by the tight-binding potential as follows:

$$\Phi_{\text{total}} = \sum_{i=1}^{N} \Phi_{ij}$$

$$= \sum_{i=1}^{N} \left\{ -\left[\sum_{j} \xi^2 \exp\left(-2q\left(\frac{r_{ij}}{r_o} - 1 \right) \right) \right]^{1/2} \right. \tag{1}$$

$$\left. + A \exp\left[-p\left(\frac{r_{ij}}{r_o} - 1 \right) \right] \right\},$$

where the subscripts i and j represent atom i and atom j, respectively, ξ is an effective hopping integral, r_{ij} is the distance between atoms i and j and r_0 is the first-neighbors' distance. The total band energy is characterized by the second moment of the d-band density of state and is shown in the first part of the potential function. Meanwhile, the second part reveals a modified form of the original tight-binding potential. The free parameters of A, ξ, p and q are fitted to the experimental values of cohesive energy, lattice parameters (by the constraint on the atomic volume), and independent elastic constants for each pure system and for alloys. The interaction force F_i on atom i is derived from the equation (1), can be expressed as

$$F_i = -\sum_{j \neq i}^{N} \left(\frac{\partial \Phi_{ij}}{\partial r_{ij}} + \frac{\partial \Phi_{ij}}{\partial r_{ij}} \right) = m_i \frac{d^2 r_i(t)}{dt^2}, \tag{2}$$

where m_i is the mass of atom i, r is the position of atom i and N is the total number of atoms. By using equation (2), the resultant forces of each individual atom can be calculated at each time step. The parametric values of the tight-binding potential for the present simulation models are adopted from Cleri *et al.* [46].

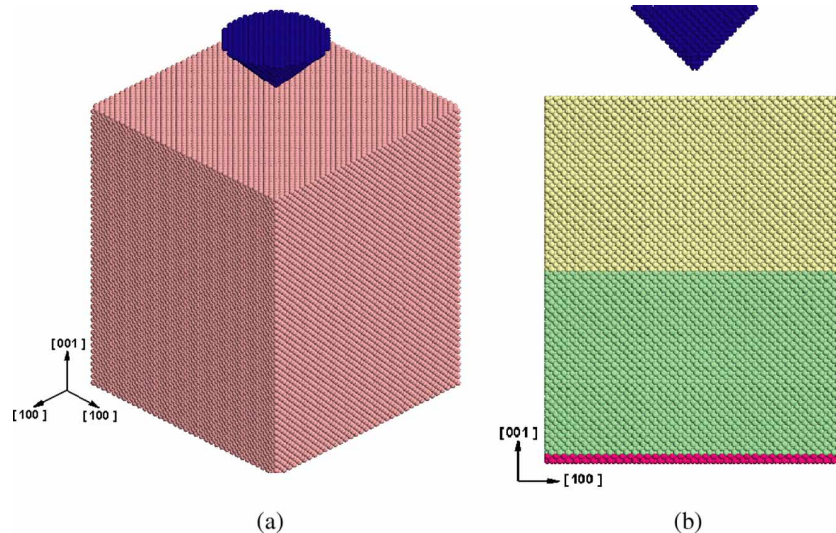Figure 1. Simulated nickel models of both the material and functional configurations. Figure 1(a) is the material configuration of the three-dimensional view; the blue colour is the tip, the pink are the nickel atoms. Figure 1(b) is the functional configuration from the lateral view; the blue and red are the rigidity atoms, the green are the thermostat atoms, and the yellow are the Newtonian atoms.

MD simulations of nanoindentation comprise the equilibrium and indentation stages. In the equilibrium stage, the tip and the substrate surface are first positioned 10 Å apart in order to avoid the effect of attractive force which occurs as they gradually approach each other. The initial positions of tip and substrate atoms are prescribed in accordance with their crystalline structures, respectively. The initial velocities are assigned from a randomised producer, and are adjusted according to the rescaling method [44] in order to achieve a constant system temperature. After being held at the initial position for a period of time, both the tip and substrate are relaxed to their equilibrium configuration as a result of the interatomic forces acting on each individual atom. In the second indentation stage of MD simulations, the indentation is modelled by moving the tip 25 Å downward at a constant speed of 5 m/s, and then retracting the tip back to its original position at the same speed. In both stages, the time integration of motion is performed by applying the velocity-Verlet algorithm [44] to the corresponding data obtained in the previous step in order to derive the new position and velocity vectors of the substrate atoms. The system temperature of simulated models is kept at 300 K during the entire process. The size of the incremental time steps employed in the computations must be smaller than the thermal motion periods in the simulated system, but not so small as to be affected by the accumulations of inevitable round-off errors during the computational process. In the present computations, a compromised choice of time step $\Delta t = 1$ fs is thus employed.

It should be noted that nanoindentation experiments are performed at much slower rates than MD simulations ($10^{-6} - 10^{-9}$ m/s); however, if conducted at these rates, MD simulations would take extremely long processing times even with the fastest microprocessors [41]. Due to computing power limitations, the speeds of the indenter tip reported in the references are on an order of $1 - 100$ m/s for most MD simulations of nanoindentation [47]. Although the indentation speed in our simulations is several orders of magnitude higher than typical experimental values, it is sufficiently slow to allow equilibrium of the indentation system, and allow any excess energy arising from the motion of the indenter to dissipate by means of Nosé-Hoover thermostat, which permits the indentation system to become a quasi-static state at each time step during nanoindentation [48]. Nevertheless, the sensitivity of the simulated results to the indentation velocity must be considered before the simulated and experimental results can be directly compared. A number of studies have attempted to do so. Liang *et al.* [49] performed MD simulations to study dislocation nucleation in the initial stage during nanoindentation. With respect to the influence of indenter velocity on the dynamic effect of the material indentation behaviour, they found that a higher indentation velocity in MD simulation leads to a higher strength, while the relationship between applied load and indentation depth shows little change.

At the same time, the ensuing dislocation structures do not differ substantially. More importantly, the indentation curves for different velocities will quickly converge as the velocity decreases and approaches approximately 3 m/s. In fact, no obvious difference is apparent when the velocity is below 3 m/s. This discovery can be understood from the research of Yamakov *et al.* [50], which uses MD simulations to investigate the dislocation processes in the deformation of nanocrystalline aluminium. They found that the typical dislocation-glide velocities of FCC nanocrystalline aluminium are about 500 m/s under strain rates of $10^7 \, \mathrm{s}^{-1}$ in the [100] direction, which are well below both the velocity of sound at about 3664 m/s, and the experimental value of 3050 m/s. Moreover, Fang *et al.* [51] utilized MD simulation to analyse the indenter velocity effects on a single crystal copper substrate. One of the results for the effect of indenter velocity on material properties reveals that the critical velocity of the indenter necessary to cause an increase in Young's modulus and in hardness is about 80 m/s. The above-mentioned references suggest that the indenter velocity of 5 m/s adopted in our simulations is suitable to observe and describe the plastic deformation behaviour and the material properties under nanoindentation.

3. Results and discussion

3.1 Plastic deformation characteristic during nanoindentation

The indentation curves of the tip force and the indentation depth for three nickel substrates with different crystallographic surfaces of (100), (110) and (111) orientations are shown in figure 2(a)–(c). The vertical axis represents the value of the tip force, defined as the resultant force at the indenting direction exerted upon the tip by nickel atoms, and the horizontal axis represents the indentation depth. The height of the tip is set to zero indentation depth when the atoms of the tip start interacting with the nickel atoms of the substrate. The positive and negative values of the tip force represent the repulsive and attractive force between the tip and the nickel substrate, respectively. For each crystallographic surface, because the interaction between two atoms is attractive as they gradually approach each other, the tip force is negative in the beginning of the indenting. As the tip increases its indentation depth into the surface, attractive force will convert into repulsive force.

In figure 2, it is clearly evident that in the course of the indenting process, the value of the tip force imposed on the nickel (100) substrate varies more significantly, while the values of tip forces exerted on nickel (110) and (111) substrates appear to monotonically increase with the indentation depth. For convenience in describing the variations of tip force with the indentation depth in figure 2, labels (1)–(18) are used to explain the characteristic variations of the indentation curves.
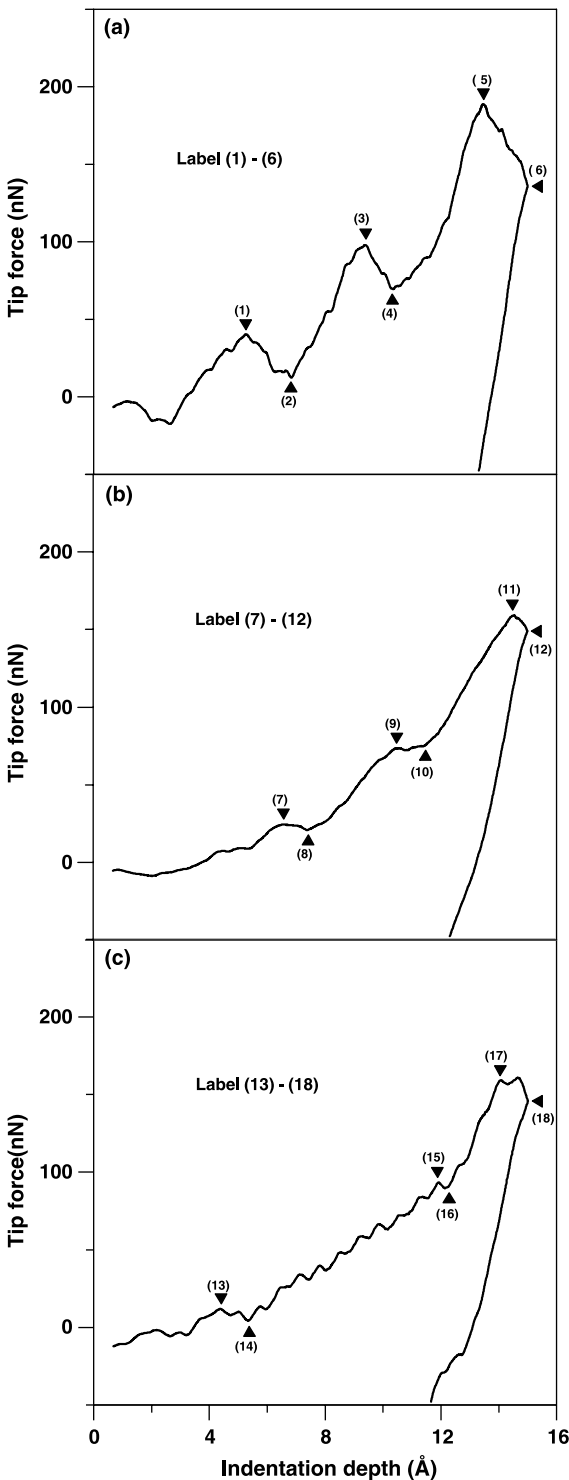
Figure 2. Indentation curves of the nickel substrates. Figure 2(a)–(c) are the three indentation curves with (100), (110) and (111) orientation surfaces, respectively. Labels (1)–(18) indicate the local peaks and local minimums, and correspond to the morphologies in figure 3–5.

Each label marks the characteristic indentation depth at which the tip force displays relatively obvious variation. The corresponding morphologies, as well as the distributions of atomic normal stress on indentation direction at these labels are shown in figures 3–5. Because the coordination number of a nickel atom in a perfect FCC

crystalline material is 12, nickel atoms with a coordination number lower than 12 under indentation are shown during the evolution of the deformation and relaxation of the substrates [52]. In addition, atomic-level stress is also used to monitor the evolution of the structure relaxation in figures 3–5. The atomic stress is obtained from the following formula [53]:

$$\sigma_{mn} = \frac{1}{N_R} \sum_i \left[\frac{m_i v_i^m v_i^n}{V_i} - \frac{1}{2V_i} \sum_j \frac{\partial \phi(r_{ij})}{\partial r_{ij}} \frac{r_{ij}^m r_{ij}^n}{r_{ij}} \right], \quad (3)$$

where m_i is the mass of atom i; V_i is the volume surrounding to atom i; N_R is the number of particles contained in region R, where R is defined as the region of atomic interaction; r_{ij} is the distance between atoms i and j; and r_{ij}^m and r_{ij}^n are two components of the vector from atom i to j. The first term of the bracketed section of equation (3) represents the kinetic effect associated with atomic motion, and will be affected by temperature. The second term is related to the interactive forces and the distance between the atoms. V_i is also named Voronoi volume, constructed by the perpendicular planes which bisect the lines between atom i and all its neighbour atoms. However, it is time-consuming to obtain the Voronoi volume of each atom, so Srolovitz [54] has used the following formulation to obtain a sphere whose volume is equal to the original Voronoi volume, namely,

$$V_i = \frac{4\pi}{3} a_i, \quad a_i = \frac{\sum_j r_{ij}^{-1}}{2\sum_j r_{ij}^{-1}}, \quad (4)$$

where a_i is the average radius of atom i, and r_{ij} is the distance between atoms i and its neighbour atom j.

Figures 3(a)–(f) depict the morphologies of nickel atoms with a coordination number lower than 12, and which correspond to the morphologies at different indentation depths on the (100) surface, marked as labels (1)–(6). The morphologies at labels (1), (3) and (5) are located at the local peaks of the (100) indentation curve, while those at labels (2), (4) and (6) are at local minimums of the tip forces. The tip force will decrease when the indentation depths increase from label (1) to (2), label (3) to (4), and label (5) to (6), because the strain energy of the substrate due to the force exerted by the tip will be released by the dislocation sliding along the {111} plane. After the release of strain energy, the indentation curve continues to rise after crossing the local minimums until the deformation energy of the next stage is released again.

As shown in figure 3(a), (c) and (e), the atomic arrangements display the homogeneous nucleation phases. Because figure 3(a) occurs at the shallow indentation stage, the formation size of nucleation is not significant in size. With the increase of indentation depth, as shown in figure 3(c) and (e), more nickel atoms nucleate around the tip, which leads to the formation of a larger nucleation. According to the stress legend in figure 3(a), (c) and (e), the nucleated atoms around the tip reveal repulsive stresses. The atomic normal stresses increase with the indentation
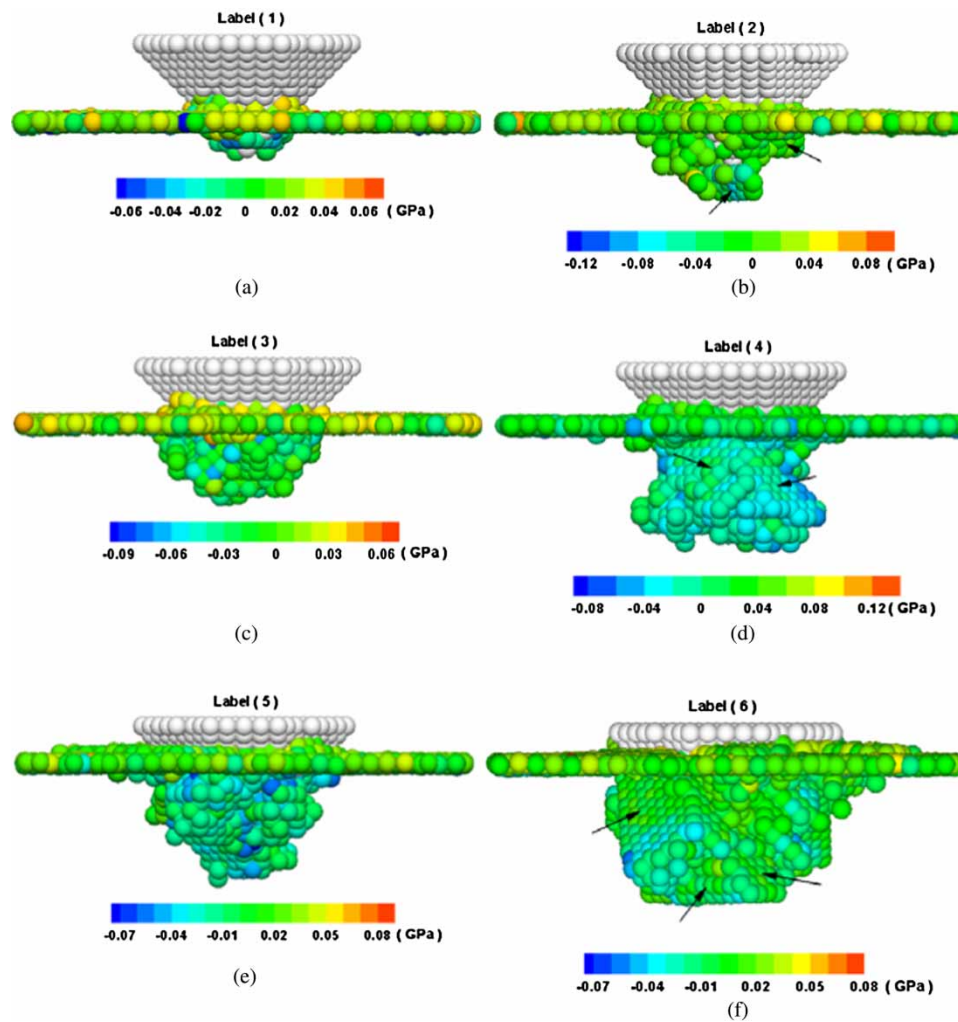
Figure 3. Three dimension snapshots of nickel (100) crystallographic substrate in different indentation depths. The colour contours represent the atomic normal stress distributions of substrate atoms. The arrows indicate the dislocation defects. The downward indentation depths in figure 3(a)–(f) are 5.1, 6.9, 9.2, 10, 13.3 and 14.9 Å, respectively.

depth, in that the maximum atomic stresses in figure 3(a), (c) and (e) for indentation depths of 5.1, 9.2 and 13.3 Å are about -0.06, -0.09 and -0.11 GPa, respectively. In contrast, the atomic arrangements in figure 3(b), (d) and (f) display the phases where dislocation from the nucleation phase takes place. In figure 3(b), because the indentation depth into the nickel substrate by the tip is not sufficient, the areas of the sliding planes are relatively small. With increase of the indentation depth, as shown in figure 3(d) and (f), the dislocation defects gradually enlarge, which results in larger areas of sliding planes. From the displays of the stress legend in figure 3(b), (d) and (f), it can be seen that the distributions of the atomic normal stress values on the {111} sliding planes are close to the zero value after the relaxation period, where strain energy is released.

Figure 4(a)–(f) and figure 5(a)–(f) also depict the morphologies of nickel atoms with the coordination number lower than 12, and which correspond to the morphologies at different indentation depths on both (110) and (111) surfaces at labels (7)–(12) and labels (13)–(18), respectively. The morphologies at labels (7), (9) and (11)

are located at the local peaks of the (110) indentation curve, while those at labels (8), (10) and (12) are at local minimums of the tip forces. Similarly, the morphologies at labels (13), (15) and (17) are located at the local peaks of the (111) indentation curve, while those at labels (14), (16) and (18) are at local minimums of the tip forces. Figure 2 shows the decrease in tip force from the local peaks to the local minimums between labels (7) and (8), labels (9) and (10), and labels (11) and (12); as well as labels (13) and (14), labels (15) and (16), and labels (17) and (18). This because the strain energy of the substrate due to the exertion of the tip is released by the dislocation along the {111} sliding plane.

The strain energy can be examined in further detail in figures 4 and 5. As previously noted, in figure 4(a), (c), and (e), the atomic arrangements display the homogeneous nucleation phases, and the formation size of nucleation increases with the increase of indentation depth. The nucleated atoms around the tip reveal the repulsive stresses, and the atomic normal stresses increase with the increase of indentation depth. The maximum atomic stresses in
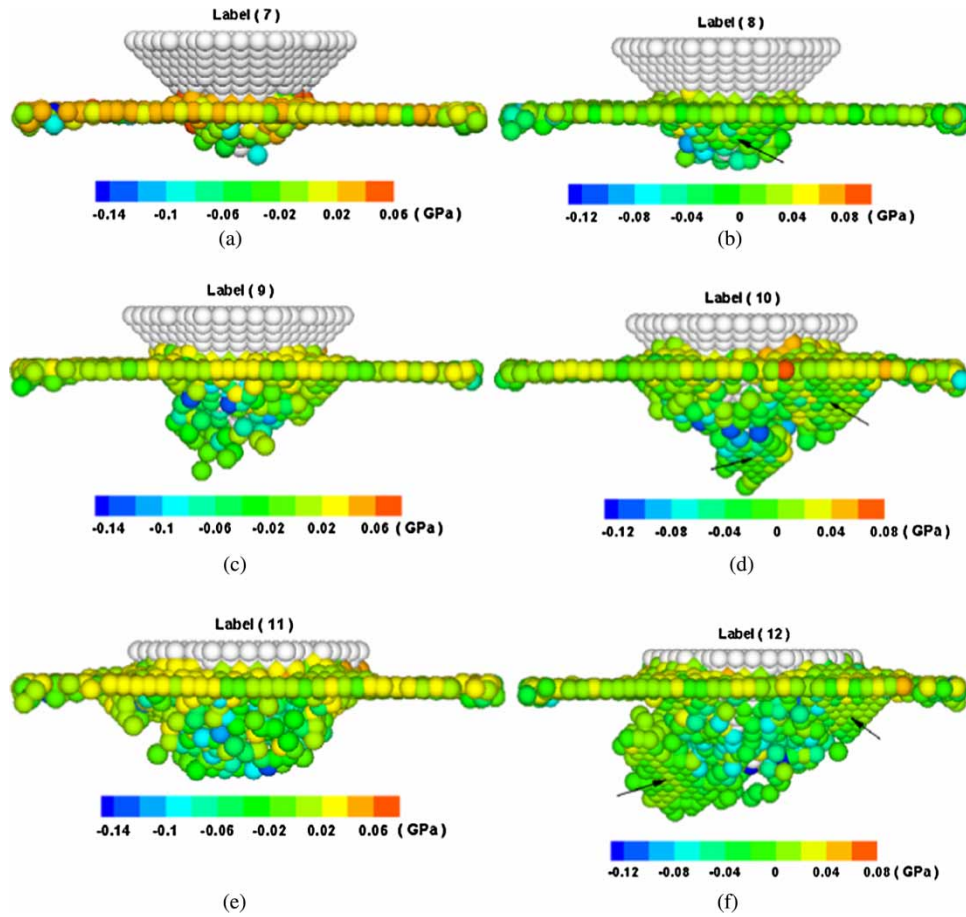
Figure 4. Three dimension snapshots of nickel (110) crystallographic substrate in different indentation depths. The colour contours represent the atomic normal stress distributions of substrate atoms. The arrows indicate the dislocation defects. The downward indentation depths in figure 4(a)–(f) are 6.5, 7.4, 10.4, 10.9, 14.3 and 14.9 Å, respectively.

figure 4(a), (c), and (e) are about -0.08, -0.11 and -0.12 GPa. In figure 4(b), (d), and (f), the atomic structures display the dislocation defect phases, and the areas and quantities of the sliding planes increase with the increase of indentation depth, while the distributions of the atomic normal stress values on the {111} sliding planes in figure 4(b), (d), and (f) are close to the zero value. In figure 5(a)–(f), the deformation evolution and atomic stress state of the (111) substrate during indentation are similar to figure 3(a)–(f) and figure 4(a)–(f). The maximum values of atomic stress in figure 5(a), (c) and (e) are about -0.09, -0.11 and -0.12 GPa, while the distributions of the atomic normal stress values on the {111} sliding planes in figure 5(b), (d), and (f) are close to the zero value. From the previously mentioned results shown in figures 3–5, the plastic deformation characteristics corresponding to the distributions of atomic normal stress illustrate that the strain energy of the substrate exerted by the tip is stored by the formation of the homogeneous nucleation in one phase, and is dissipated by the dislocation sliding of the {111} plane in the following phase.

Furthermore, the series of drop phenomena during nanoindentation found in the three indentation curves in figure 2 correspond to the dislocation nucleation patterns presented in figures 3–5, and which conform to the related

research of MD simulations for the FCC single crystal metals of nanoindentation [47,55–58]. These patterns are identified in the (100) surface orientation substrate as prismatic dislocation loop [55], and in the (111) surface orientation substrate as the dislocation defects of the tetrahedral sessile lock [47], the three-fold symmetry dislocation [56–57] or the three unique {111} sliding planes [58]. Finally, because of different orientation surfaces in the three nickel substrates, the numbers of slip angles of {111} sliding planes in the three nickel substrates are different. The numbers of slip angles for the three nickel substrates can be calculated from Wulff net projection [59]. The slip angle of {111} sliding planes in the (100) substrate is 54.7°, and the slip angles of {111} sliding planes in the (110) substrate are 35.3 and 90°, while the slip angles of {111} sliding planes in the (111) substrate are 0, 70.5 and 109.5°. From these results of slip angle numbers of {111} sliding planes in the three nickel substrates corresponding to the trend variations of the indentation curves, it can be found that the steep variations of the indentation curve from the local peaks to the local minimums are affected by the numbers of slip angles of the {111} sliding plane. Because the steep variations of the indentation curve are related to the plastic deformation ability of the material substrates during nanoindentation,
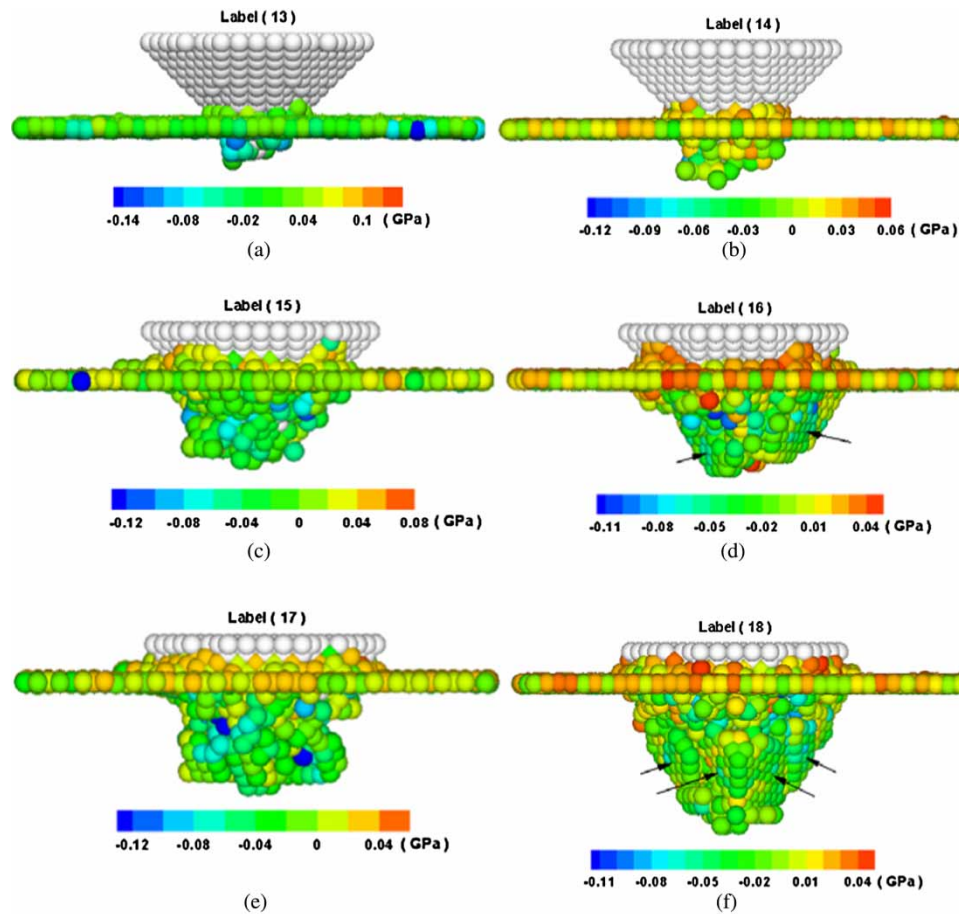
Figure 5.   Three dimension snapshots of nickel (111) crystallographic substrate in different indentation depths. The colour contours represent the atomic normal stress distributions of substrate atoms. The arrows indicate the dislocation defects. The downward indentation depths in figure 5(a)−(f) are 4.3, 5.3, 11.9, 12.2, 14.7 and 14.9 Å, respectively.

the steep variations of the three indentation curves in figure 2 decrease when the numbers of slip angles of the {111} sliding plane increase in the three nickel substrates. This indicates that the (111) nickel substrate exhibits more dislocation activity owing to the maximum number of three slip angles, and the (100) nickel substrate exhibits less dislocation activity due to the minimum number of only one slip angle, with the dislocation activity of the (110) nickel substrate between the (111) and (100) nickel substrates as a result of two slip angles.

3.2 Pile-up patterns after nanoindentation

The actual contact area between the tip and the specimen is determined by the shape of the out-of-plane displacement zone, which will affect the quantitative analysis of the material property measurements. Therefore, the pile-up patterns produced after nanoindentation are also observed in the present MD simulations. As shown in figure 6, the MD simulations show different surface profiles around the simulated tip for the three different surface orientations of
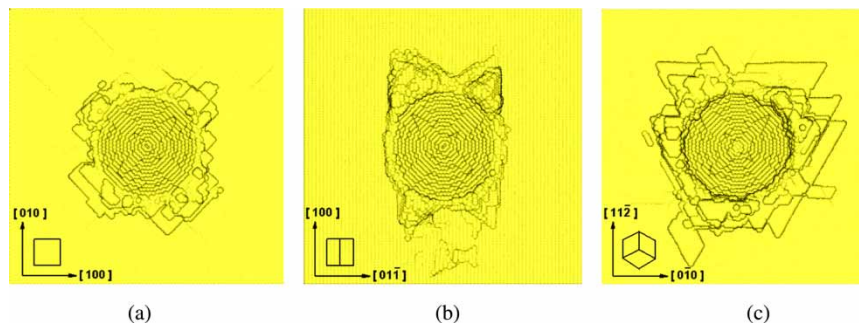

Figure 6.   Pile-up patterns of the top view for the (a) (100), (b) (110) and (c) (111) oriented nickel single crystal surfaces obtained from the present MD simulation.

nickel substrates. The MD simulated contour plots of the out-of-plane displacement profiles display the pile-up patterns on the surface of the (100)-, (110)- and (111)-oriented surfaces. The MD simulated contour maps for the hillocks of pile-up patterns in figure 6(a)–(c) display a crisscross of two-fold symmetry for the (100)-oriented crystal, an edge formed by two meeting points of the two-fold symmetry for the (110)-oriented crystal, and a hexagon of three-fold symmetry for the (111)-oriented crystals, respectively. The pile-up contour maps for the three crystallographic nickel substrates in figure 6 show that the pile-up dislocations are significantly affected by different surface orientations. For nickel materials, Huang *et al.* [60] utilized micro-indentation to investigate the surface deformation mode of a NiTi shape-memory alloy after the indentation and a subsequent thermal cycle. In addition, Barshilia *et al.* [61] employed low-angle X-ray diffraction and atomic force microscopy (AFM) to study structural characterization and nano-hardness measurements on Cu/Ni multilayer coatings. The results in references [60,61] reveal that the pile-up patterns of the nickel-based material are visible around the indentation surface under nanoindentation, with the resultant indents "piling-up" above room temperature, and "sinking-in" at low temperatures. Corresponding to the pile-up investigations of references [60,61], our results show that the pile-up of nickel materials are produced by the tip around the indentation surface after indentation, which further confirms our present simulations, which are modelled at room temperature.

In order to further verify the simulated pattern accuracy, the pile-up patterns of the present simulations for the three crystallographic nickel substrates are compared with the research literature for both finite element method (FEM) simulations and experimental tests [40]. Figure 2 of reference [40] shows FEM simulation contour plots of the out-of-plane displacement profiles on (100)-, (110)- and (111)-oriented surfaces for single crystal copper samples. Similarly, figure 3 of reference [40] shows the AFM images for experimental nanoindentation tests on the same orientation crystallographic surfaces and the same single crystal copper material. A comparison of pile-up patterns in the present simulations to reference [40] shows that the contour shape of the MD simulation is similar to both the FEM simulation and experimental results. The differences for the detailed contour are attributable to the fact that the maximum indentation depth used in the present simulations is very shallow as compared with both figures 2 and 3 of reference [40]. In addition, the small scale of pile-up patterns in MD simulations provides detail that is not present in FEM simulations and experimental tests. However, the pile-up patterns of the three nickel substrates in the present MD simulations are in good agreement with the FEM simulations and experimental tests in reference [40], which prove that the crystalline nickel materials demonstrate the pile-up phenomenon by nanoindentation on the nano-scale similar to the pile-up patterns of the bulk FCC materials on the micron-scale.

Finally, because the hillocks and extensions of the pile-up pattern on the indentation surface represent a dislocation spreading of the materials, both the hillock heights and extension lengths of the pile-up pattern in figure 6 can provide more information about plastic deformation ability. First, the heights of the largest hillock around the edge of the indentation hole in figure 6(a)–(c) are about 1.6, 2.7 and 3.2 Å, respectively, and are clearly visible from the pile-up patterns in figure 6. Secondly, the lengths of the longest extension perpendicular to the edge of indentation hole in figure 6(a)–(c) are about 2.7, 4.6 and 5.7 Å, respectively, and are also clearly visible from the pile-up patterns of figure 6. In the three crystallographic nickel substrates, the (111) surface orientation exhibits the most pile-up dislocation spreading, the (100) surface orientation exhibits the least, with the extent of pile-up dislocation spreading in the (110) surface orientation in between. These results are consistent with the results found in reference [41] by Komanduri *et al.*, who found that the amount of plastic deformation and the pile-up dislocation of the aluminium substrate around the indenter during nanoindentation were observed to be at the maximum on the (111) surface orientation. While Komanduri *et al.*'s study [41] provides pile-up details for the (111) orientation, our study presents not only the pile-up patterns for (100), (110) and (111) orientations, but also the corresponding indentation curves which display the effects of dislocation spreading. The fact that the (111) surface orientation exhibits more pile-up dislocation spreading can be seen in the numerous small variations on its indentation curve, as opposed to the steep variations found on the (100) and (110) indentation curves in figure 2.

3.3 Extracted material properties from nanoindentation

In order to further understand the influence of three crystallographic orientation surfaces on the mechanical properties, the formulations developed by Oliver [62] are used to calculate the hardness and Young's modulus of the three crystallographic substrates. The Young's modulus is first calculated by the reduced elastic modulus E_r, which takes into account the combined elastic effects of indentation tip and substrates, as follows:

$$E_r = \frac{\sqrt{\pi}S}{2\sqrt{A}}, \qquad (5)$$

where E and ν are the Young's modulus and Poisson's ratio with the subscripts s and i representing the sample and tip, respectively. The material properties of the tip used in this study are $E_i = 1141$ GPa and $\nu_i = 0.07$ [62–63]. The hardness is thus calculated from the equation below as follows:

$$\frac{1}{E_r} = \frac{\left(1 - \nu_s^2\right)}{E_s} + \frac{\left(1 - \nu_i^2\right)}{E_i}, \qquad (6)$$

where E and ν are the Young's modulus and Poisson's ratio with the subscripts s and i representing the sample

Table 1.　A comparison of the material properties of three nickel crystallographic substrates with (100), (110) and (111) orientation.

	Hardness (GPa)			Young's modulus (GPa)		
Surface orientation	(100)	(110)	(111)	(100)	(110)	(111)
MD simulation results	16.7	15.8	15.1	288.07	264.51	224.26
MD simulation values in reference literature	14.8 [55]	–	–	–	–	–
Experimental values in the reference literature (surface orientation unknown)		3.5–8.4 [64,65,67–70]			164–218 [65,66,68,71]	

and tip, respectively. The hardness is thus calculated from the equation below as follows:

$$H = \frac{P_{\max}}{A_p} = \frac{P_{\max}}{A(h_c)}, \qquad (7)$$

where $P_{\max}$ is the maximum load of the tip at the maximum depth, A_p is the contact area, h_c is the contact depth, and may be expressed as

$$h_c = h_{\max} - \varepsilon \cdot \frac{P_{\max}}{S}, \qquad (8)$$

where ε is the geometric constant of the tip. For the conical tip, it is given a value of 0.72; for the flat punch, it is given a value of 1; and for the paraboloid of revolution, a value of 0.75. After the calculations to the hardness and Young's modulus, the calculated results are compared with the values reported in literature, as shown in table 1.

The hardness values found in table 1 for the (100), (110) and (111) nickel substrates obtained from our simulations at the maximum indentation depth 1.5 nm are 16.7 GPa, 15.8 and 15.1 GPa, respectively. Similarly, in other simulation research, the hardness value obtained from Saraev *et al.* [55] using MD simulation of nanoindentation at the same indentation depth 1.5 nm is 14.8 GPa, whereas the hardness values of nickel material obtained from nanoindentation experiments as reported in reference documents are in the range of 3.5–8.4 GPa [64,65,67–70]. Secondly, regarding the Young's modulus values in table 1, the values of the (100), (110) and (111) nickel substrates obtained from our simulations are 288.07, 264.51, and 224.26 GPa, respectively. The Young's modulus values of nickel material obtained from nanoindentation experiments as reported in reference literature are in the range of 164–218 GPa [65,66,68,71]. As is evident, the hardness values of the three nickel substrates in our simulations are close to the hardness values produced in MD simulations under similar simulation conditions, yet higher than the experimental values as reported in the reference literature. Similarly, the Young's modulus values of the present simulations for the three nickel substrates are also higher than the experimental values reported in the reference literature. The differences of both the hardness and Young's modulus values between the experimental and the simulated results were attributed to a number of factors: the indentation size effect [41,55,72–75], the difference in specimen scale between experiment and simulation that results in a restriction of dislocation activity in MD simulations [76–78], the higher strain rate due to the higher indenter velocity in MD simulations as compared with

experiments [51,79], the experimental scatter and surface roughness in experimental specimens [80], the true contact area value underestimation due to the pile-up phenomenon in MD simulations [73], and the different crystal texture between the perfect mono-crystalline used in MD simulations and experimental specimens which contain a variety of defects [75–78,81]. Although the material properties of both the hardness and Young's modulus values in our simulations are higher than the experimental values of the reference documents, the simulated values for the hardness and Young's modulus obtained from our simulations are still within a reasonable range.

Furthermore, the hardness values of the three crystallographic nickel substrates calculated from the present simulations show that the hardness value of the (100) substrate is greatest, while the hardness value of the (110) substrate is smaller than the (100) substrate, and the hardness value of the (111) substrate is smallest. This is due to the fact that the (100) substrate has only one slip angle of the {111} sliding planes that occur during nanoindentation, which leads to a lower ability for plastic deformation, and results in a higher hardness value. In contrast, because the (111) substrate has three slip angles of the {111} sliding planes that occur during nanoindentation, the (111) substrate exhibits a better ability for plastic deformation, which leads to a lower hardness value. The (110) substrate has two slip angles of the {111} sliding planes that occur during nanoindentation, so the ability for plastic deformation is between the (100) and (111) substrate values, which leads to a hardness value in between the (100) and (110) substrates. The (100) surface orientation of FCC materials exhibits the maximum hardness value for the three crystallographic surface orientations, also shown in the research previously mentioned [41]. The results in reference [41] for the influence of orientation effect on the hardness values reveal that the hardness of the (100) crystallographic aluminium substrate exhibits the maximum value under nanoindentation, and represents the least anisotropy on the [001] direction. The results in our simulations for the hardness value of the (100) nickel substrate in the three surface orientations are in accord with the results of reference [41]. Because the hardness values of the three nickel substrates correspond to the numbers of slip angle at the {111} sliding planes, the different slip angles lead to different dislocation activity during nanoindentation. This indicates that the hardness of FCC nickel material on the nano-scale is significantly affected by crystallographic surfaces with different orientations.

Finally, the Young's modulus values of the three crystallographic nickel substrates calculated from the present simulations show that the Young's modulus value of the (100) substrate is greatest, while the Young's modulus value of the (110) substrate is smaller than the (100) substrate, and the Young's modulus value of the (111) substrate is smallest. Because the Young's modulus is only related to the capability for elastic deformation, the material's resistance to elastic deformation at the moment of initial unloading is completely provided by the constitutional strength of atomic bonding. Therefore, a comparison of Young's modulus for the three nickel substrates can be drawn from the average cohesive energy between nickel atoms, as shown in figure 7, with the horizontal axis representing the indentation depth, and the vertical axis representing the average value of cohesive energy for all atoms of the nickel substrate, defined as the atomic bonding strength between nickel atoms. In figure 7, it can be clearly seen that throughout the entire indentation process, the (100) substrate has the maximum value of cohesive energy, while the cohesive energy of the (110) substrate is smaller than the (100) substrate from the indentation, and the cohesive energy of the (111) substrate always maintaining the minimum value. The Young's modulus values of the three nickel substrates have a proportional relationship to cohesive energy, which reveals that the elastic modulus of FCC nickel material on the nano-scale is significantly affected by the different crystallographic orientation surfaces.

4. Conclusions

In the present study, MD simulations have been performed on the crystallographic nickel substrates with (100), (110)
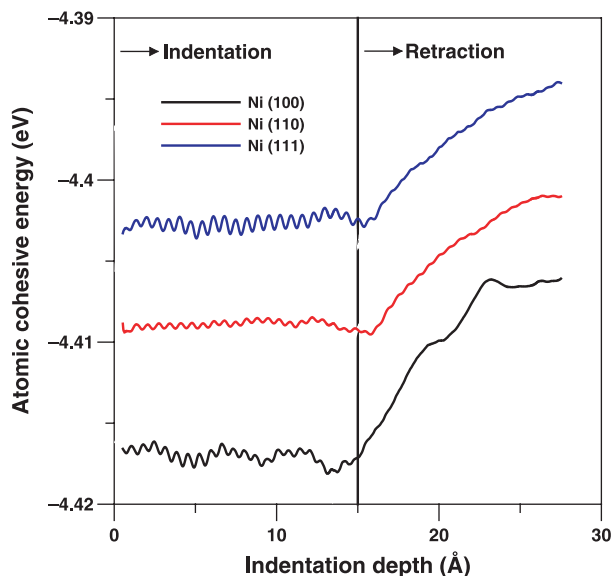

Figure 7. The cohesive energy curves between nickel atoms of the crystallographic nickel substrates with (100), (110) and (111) orientation surfaces.

and (111) orientation surfaces under nanoindentation. Analysis was performed on the plastic deformation characteristics corresponding to the atomic normal stress variations during nanoindentation, the pile-up patterns after nanoindentation, and the influence of plastic deformation characteristics on the material properties due to different crystallographic orientations of the nickel substrates. From the present results of nanoindentation, the principal conclusions of the present studies can be summarized as follows:

(1) From the plastic deformation characteristics corresponding to the atomic normal stress variations during nanoindentation, the strain energy of the substrate exerted by the tip is stored by the formation of homogeneous nucleation, and is dissipated by the dislocation sliding of the {111} plane.
(2) The steep variations of the indentation curve from the local peaks to the local minimums are affected by the numbers of slip angles of the {111} sliding plane, due to the fact that the steep variations on the three indentation curves decrease as the numbers of slip angles of the {111} sliding plane increases in the three nickel substrates.
(3) The pile-up patterns of the three nickel substrates in the present simulations are in good agreement with the reported literature, which prove that the crystalline nickel materials also produce the pile-up phenomenon by nanoindentation under the nano-scale, and which are similar to the pile-up patterns of the bulk FCC materials on the micron-scale.
(4) The (111) surface orientation exhibits the most pile-up dislocation spreading, the (100) surface orientation exhibits the least, with the extent of pile-up dislocation spreading in the (110) surface orientation in between. The results are consistent with the reported literature, and are in accordance with the steep variations of the three indentation curves.
(5) Owing to a number of factors as reported in the literature, the present simulation values of both the hardness and Young's modulus are higher than the literature values; however, the present simulation values are within the reasonable range.
(6) The effects of surface orientation in material properties of FCC nickel material on the nano-scale are observable through the slip angle numbers which influence hardness values, as well as the cohesive energy of different crystallographic surfaces that indicate Young's modulus.

Acknowledgements

References

[1] J.F. Lin, C.C. Wei, Y.K. Yung, C.F. Ai. The effects of hydrogenated carbon films with different film thickness and nitrogen content on specimen mechanical properties, scratch critical load, adhesion work and tribological behavior. *Diam. Relat. Mat.*, **13**, 1895 (2004).

[2] K.D. Bouzakis, S. Hadjiyiannis, G. Skordaris, I. Mirisidis, N. Michailidis, K. Efstathiou, E. Pavlidou, G. Erkens, R. Cremer, S. Rambadt, I. Wirth. The effect of coating thickness, mechanical strength and hardness properties on the milling performance of PVD coated cemented carbides inserts. *Surf. Coat. Technol.*, **177**, 657 (2004).

[3] B.C. Zhang, G. Barth, H.K. Liu, S. Chang. Characterization of nickel phosphorus surface by ToF-SIMS. *Appl. Surf. Sci.*, **231**, 868 (2004).

[4] R. Ji, T. Liew, C.H. Seek, T.C. Chong. Corrosive effect of acrylic acid on magnetic head and media of an operating hard disk drive. *Tribol. Int.*, **38**, 692 (2005).

[5] D. Son, J.J. Kim, J.Y. Kim, D. Kwon. Tensile properties and fatigue crack growth in LIGA nickel MEMS structures. *Mater. Sci. Eng. A Struct. Mater. Prop. Microstruct. Proces.*, **406**, 274 (2005).

[6] E. Slavcheva, W. Mokwa, U. Schnakenberg. Electrodeposition and properties of NiW films for MEMS application. *Electrochim. Acta*, **50**, 5573 (2005).

[7] B. Li, Q. Chen, D.G. Lee, J. Woolman, G.P. Carman. Development of large flow rate, robust, passive micro check valves for compact piezoelectrically actuated pumps. *Sens. Actuat. A Phys.*, **117**, 325 (2005).

[8] E. Gomez, E. Pellicer, M. Duch, J. Esteve, E. Valles. Molybdenum alloy electrodeposits for magnetic actuation. *Electrochim. Acta*, **51**, 3214 (2006).

[9] M. Zhao, C. Jiang, S. Li, S.X. Mao. Probing nano-scale mechanical characteristics of individual semi-conducting nanobelts. *Mater. Sci. Eng. A Struct. Mater. Prop. Microstruct. Proces.*, **409**, 223 (2005).

[10] A. Gouldstone, H.J. Koh, K.Y. Zeng, A.E. Giannakopoulos, S. Suresh. Discrete and continuous deformation during nanoindentation of thin films. *Acta Mater.*, **48**, 2277 (2000).

[11] A.A. Voevodin, M.A. Capano, S.J.P. Laube, M.S. Donley, J.S. Zabinski. Design of a Ti/TiC/DLC functionally gradient coating based on studies of structural transitions in Ti-C thin films. *Thin Sol. Films*, **298**, 107 (1997).

[12] B. Alder, T. Wainwright. Studies in molecular dynamics: I. General method. *J. Chem. Phys.*, **31**, 459 (1959).

[13] B. Alder, T. Wainwright. Studies in molecular dynamics: II. Behavior of a small number of elastic spheres. *J. Chem. Phys.*, **33**, 1439 (1960).

[14] W.G. Hoover, A.J. De Groot, C.G. Hoover, I.F. Stowers, T. Kawai, B.L. Holian, T. Boku, S. Ihara, J. Belak. Large scale elastic–plastic indentation simulations via non-equilibrium molecular dynamics. *Phys. Rev. A*, **42**, 5844 (1990).

[15] J. Belak, D.B. Boercker, I.F. Stowers. Simulation of nanometer scale deformation of metallic and ceramic surfaces. *MRS Bull.*, **18**, 55 (1993).

[16] U. Landman, W.D. Luedtke, N.A. Burnham, R.J. Colton. Atomistic mechanisms and dynamics of adhesion, nanoindentation, and fracture. *Science*, **248**, 454 (1990).

[17] U. Landman, W.D. Luedtke. Nanomechanics and dynamics of tip-substrate interactions. *J. Vac. Sci. Technol.*, **9**, 414 (1991).

[18] U. Landman, W.D. Luedtke, E.M. Ringer. Atomistic mechanisms of adhesive contact formation and interfacial processes. *Wear*, **153**, 3 (1992).

[19] U. Landman, W.D. Luedtke. Atomistic dynamics of interfacial processes: films, junctions, and nanostructure. *Appl. Surf. Sci.*, **92**, 237 (1996).

[20] R. Komanduri, N. Chandrasekaran, L.M. Raff. MD simulation of nanometric cutting of single crystal aluminum-effect of crystal orientation and direction of cutting. *Wear*, **242**, 60 (2000).

[21] R. Komanduri, N. Chandrasekaran, L.M. Raff. Effect of tool geometry in nanometric cutting: a molecular dynamics simulation approach. *Wear*, **219**, 84 (1998).

[22] S. Shimada. Molecular dynamics analysis of nanometric cutting process. *Int. J. Jpn. Soc. Precis. Eng.*, **29**, 283 (1995).

[23] T. Inamura, H. Suzuki, N. Takezawa. Cutting experiments in a computer using atomic models of copper crystal and diamond tool. *Int. J. Jpn. Soc. Precis. Eng.*, **25**, 259 (1991).

[24] K. Maekawa, A. Itoh. Friction and tool wear in nanoscale machining-molecular dynamics approach. *Wear*, **188**, 115 (1995).

[25] N. Chandrasekaran, A. Noori-Khajavi, L.M. Raff, R. Komanduri. A new method for molecular dynamics simulation of nanometric cutting. *Philos. Mag.*, **77**, 7 (1998).

[26] R. Komanduri, N. Chandrasekaran, L.M. Raff. Some aspects of machining with negative rake tools simulating grinding: an MD simulation approach. *Philos. Mag.*, **79**, 955 (1999).

[27] O. Tomagnini, F. Ercolessi, E. Tosatti. Microscopic interaction between a gold tip and lead surface. *Surf. Sci.*, **287**, 1041 (1993).

[28] D.W. Brenner, S.B. Sinnott, J.A. Harrison, O.A. Shenderova. Simulated engineering of nanostructures. *Nanotechnology*, **7**, 161 (1996).

[29] R. Rentsch, I. Inasaki. Indentation simulation on brittle materials by molecular dynamics. *SPIE*, **2596**, 214 (1995).

[30] J.A. Harrison, D.W. Brenner, C.T. White, R.J. Colton. Atomistic mechanisms of adhesion and compression of diamond surfaces. *Thin Sol. Films*, **206**, 213 (1991).

[31] W. Yan, K. Komvopoulos. Three-dimensional molecular dynamics analysis of atomic-scale indentation. *J. Tribol. Trans. ASME*, **120**, 385 (1998).

[32] J.A. Harrison, C.T. White, R.J. Colton, D.W. Brenner. Molecular dynamics simulations of atomic-scale friction of diamond surfaces. *Phys. Rev B*, **46**, 9700 (1992).

[33] A. Buldum, S. Ciraci. Contact, nanoindentation, and sliding friction. *Phys. Rev. B*, **57**, 2468 (1998).

[34] D.E. Kim, N.P. Suh. Molecular dynamics investigation of two dimensional atomic-scale friction. *J. Tribol. Trans. ASME*, **116**, 225 (1994).

[35] M. Hirano, K. Shinjo. Atomistic locking and friction. *Phys. Rev. B*, **41**, 11837 (1990).

[36] R. Komanduri, N. Chandrasekaran, L.M. Raff. Molecular dynamics simulation of atomic-scale friction. *Phys. Rev. B*, **61**, 14007 (2000).

[37] P. Walsh, R.K. Kalia, A. Nakano, P. Vashishta. Amorphization and anisotropic fracture dynamics during nanoindentation of silicon nitride: a multimillion atom molecular dynamics study. *Appl. Phys. Lett.*, **77**, 4332 (2000).

[38] P. Walsh, A. Omeltchenko, R.K. Kalia, A. Nakano, P. Vashishta. Nanoindentation of silicon nitride: a multimillion-atom molecular dynamics study. *Appl. Phys. Lett.*, **82**, 118 (2003).

[39] F.K. Mante, G.R. Baran, B. Lucas. Nanoindentation studies of titanium single crystals. *Biomaterials*, **20**, 1051 (1999).

[40] Y. Wang, D. Raabe, C. Kluber, F. Roters. Orientation dependence of nanoindentation pile-up patterns and of nanoindentation micro-textures in copper single crystals. *Acta Mater.*, **52**, 2229 (2004).

[41] R. Komanduri, N. Chandrasekaran, L.M. Raff. MD simulation of indentation and scratching of single crystal aluminum. *Wear*, **240**, 113 (2000).

[42] O. Kum. Orientation effects of elastic–plastic deformation at surfaces: nanoindentation of nickel single crystals. *Mol. Simul.*, **31**, 115 (2005).

[43] Y.R. Jeng, P.C. Tsai, T.H. Fang. Molecular dynamics studies of atomic-scale friction for roller-on-slab systems with different rolling-sliding conditions. *Nanotechnology*, **16**, 1941 (2005).

[44] D. Frenkel, B. Smit. *Understanding Molecular Simulation*, 2nd ed., (2002).

[45] S. Plimpton. Computational limits of classical molecular dynamics simulations. *J. Comput. Phys.*, **117**, 1 (1995).

[46] F. Cleri, V. Rosato. Tight-binding potentials for transition metals and alloys. *Phys. Rev. B*, **48**, 22 (1993).

[47] Y. Lee, J.Y. Park, S.Y. Kim, S. Jun, S. Im. Atomistic simulations of incipient plasticity under Al (111) nanoindentation. *Mech. Mater.*, **37**, 1035 (2005).

[48] C. Zhu, W. Guo, T.X. Yu, C.H. Woo. Radial compression of carbon nanotubes: deformation and damage, super-elasticity and super-hardness. *Nanotechnology*, **16**, 1035 (2005).

[49] H.Y. Liang, C.H. Woo, H. Huang, A.H.W. Ngan, T.X. Yu. Dislocation nucleation in the initial stage during nanoindentation. *Philos. Mag.*, **83**, 3609 (2003).

[50] V. Yamakov, D. Wolf, S.R. Phillpot, A.K. Mukherjee, H. Gleiter. Dislocation processes in the deformation of nanocrystalline aluminium by molecular-dynamics simulation. *Nature*, **1**, 1 (2002).

[51] T.H. Fang, S.R. Jian, D.S. Chuu. Molecular dynamics analysis of effects of velocity and loading on the nanoindentation. *Jpn. J. Appl. Phys.*, **41**, L1328 (2002).

[52] D. William, J.R. Callister. *Materials Science and Engineering*, 6th ed., (2003).

[53] N. Miyazaki, Y. Shiozaki. Calculation of mechanical properties of solids using molecular dynamics. *JSME Int. J. Ser. A Solid Mech. Mat. Eng.*, **39**, 606 (1996).

[54] D. Srolovitz, K. Maeda, V. Vitek, T. Egami. Structural defects in amorphous solids: statistical analysis of a computer model. *Philos. Mag.*, **44**, 847 (1981).

[55] D. Saraev, R.E. Miller. Atomic-scale simulations of nanoindentation-induced plasticity in copper crystals with nanometer-sized nickel coatings. *Acta Mater.*, **54**, 33 (2006).

[56] T. Zhu, J. Li, K.J. Van Vliet, S. Ogata, S. Yip, S. Suresh. Predictive modeling of nanoindentation-induced homogeneous dislocation nucleation in copper. *J. Mech. Phys. Solids*, **52**, 691 (2004).

[57] K.J. Van Vliet, J. Li, T. Zhu, S. Yip, S. Suresh. Quantifying the early stages of plasticity through nanoscale experiments and simulations. *Phys. Rev. B*, **67**, 104105 (2003).

[58] C.L. Kelchner, S.J. Plimpton, J.C. Hamilton. Dislocation nucleation and defect structure during surface indentation. *Phys. Rev. B*, **58**, 11085 (1998).

[59] D. Hull, D.J. Bacon. *Introduction to Dislocations*, 4th ed., (2001).

[60] W.M. Huang, J.F. Su, M.H. Hong, B. Yang. Pile-up and sink-in in micro-indentation of a NiTi shape-memory alloy. *Scr. Mater.*, **53**, 1055 (2005).

[61] H.C. Barshilia, K.S. Rajam. Characterization of Cu/Ni multilayer coatings by nanoindentation and atomic force microscopy. *Surf. Coat. Technol.*, **155**, 195 (2002).

[62] W.C. Oliver, G.M. Pharr. An improved technique for determining hardness and elastic modulus using load and displacement sensing indentation experiments. *J. Mater. Res.*, **7**, 1564 (1992).

[63] H. Ni, X. Li, H. Gao, T.P. Nguyen. Nanoscale structural and mechanical characterization of bamboo-like polymer/silicon nanocomposite films. *Nanotechnology*, **16**, 1746 (2005).

[64] R.A. Mirshams, R.M. Pothapragada. Correlation of nanoindentation measurements of nickel made using geometrically different indenter tips. *Acta Mater.*, **54**, 1123 (2006).

[65] L. Riester, P.J. Blau, E. Lara-Curzio, K. Breder. Nanoindentation with a Knoop indenter. *Thin Sol. Films*, **377**, 635 (2000).

[66] J.L. Bucaille, S. Stauss, P. Schwaller, J. Michler. A new technique to determine the elastoplastic properties of thin metallic films using sharp indenters. *Thin Sol Films*, **447**, 239 (2004).

[67] R. Schwaiger, B. Moser, M. Dao, N. Chollacoop, S. Suresh. Some critical experiments on the strain-rate sensitivity of nanocrystalline nickel. *Acta Mater.*, **51**, 5159 (2003).

[68] J.A.D. Jensen, P.O.A. Persson, K. Pantleon, M. Oden, L. Hultman. Electrochemically deposited nickel membranes; process–microstructure–property relationships. *Surf. Coat. Technol.*, **172**, 79 (2003).

[69] R. Mitra, R.A. Hoffman, A. Madan, J.R. Weertman. Effect of process variables on the structure, residual stress and hardness of sputtered nanocrystalline nickel films. *J. Mater. Res.*, **16**, 1010 (2001).

[70] R.A. Mirshams, P. Padama. Nanoindentation of nanocrystalline Ni with geometrically different indenters. *Mater. Sci. Eng. A Struct. Mater. Prop. Microstruct. Proces.*, **372**, 252 (2004).

[71] M. Kopycinska-Muller, R.H. Geiss, J. Muller, D.C. Hurley. Elastic-property measurements of ultrathin films using atomic force acoustic microscopy. *Nanotechnology*, **16**, 703 (2005).

[72] D. Mulliah, S.D. Kenny, E. McGee, R. Smith, A. Richter, B. Wolf. Atomistic modelling of ploughing friction in silver, iron and silicon. *Nanotechnology*, **17**, 1807 (2006).

[73] R. Smith, D. Christopher, S.D. Kenny. Defect generation and pileup of atoms during nanoindentation of Fe single crystals. *Phys. Rev. B*, **67**, 245405 (2003).

[74] P. Walsh, A. Omeltchenko, R.K. Kalia, A. Nakano, P. Vashishta. Nanoindentation of silicon nitride: a multimillion-atom molecular dynamics study. *Appl. Phys. Lett.*, **82**, 118 (2003).

[75] R. Astala, M. Kaukonen, R.M. Nieminen. Nanoindentation of silicon surfaces: molecular-dynamics simulations of atomic force microscopy. *Phys. Rev. B*, **61**, 2973 (2000).

[76] T.H. Fang, W.J. Chang, C.I. Weng. Nanoindentation and nanomachining characteristics of gold and platinum thin films. *Mater. Sci. Eng. A Struct. Mater. Prop. Microstruct. Proces.*, **430**, 332 (2006).

[77] A. Noreyan, J.G. Amar, I. Marinescu. Molecular dynamics simulations of nanoindentation of beta-SiC with diamond indenter. *Mater. Sci. Eng. B Solid State Mater. Adv. Technol.*, **117**, 235 (2005).

[78] T.H. Fang, C.I. Weng, J.G. Chang. Molecular dynamics analysis of temperature effects on nanoindentation measurement. *Mater. Sci. Eng. A-Struct. Mater. Prop. Microstruct. Process*, **357**, 7 (2003).

[79] J.Y. Hsieh, S.P. Ju, S.H. Li, C.C. Hwang. Temperature dependence in nanoindentation of a metal substrate by a diamondlike tip. *Phys. Rev. B*, **70**, 195424 (2004).

[80] S.R. Jian, T.H. Fang, D.S. Chuu, L.W. Ji. Atomistic modeling of dislocation activity in nanoindented GaAs. *Appl. Surf. Sci.*, **253**, 833 (2006).

[81] A. Richter, R. Ries, R. Smith, M. Henkel, B. Wolf. Nanoindentation of diamond, graphite and fullerene films. *Diam. Relat. Mat.*, **9**, 170 (2000).